Path profiles of Cn2 derived from radiometer temperature measurements and geometrical ray tracing

Brian E. Vyhnalek

National Aeronautics and Space Administration
Glenn Research Center
Cleveland, OH, USA

ABSTRACT

Atmospheric turbulence has significant impairments on the operation of Free-Space Optical (FSO) communication systems, in particular temporal and spatial intensity fluctuations at the receiving aperture resulting in power surges and fades, changes in angle of arrival, spatial coherence degradation, etc. The refractive index structure parameter C_n^2 is a statistical measure of the strength of turbulence in the atmosphere and is highly dependent upon vertical height. Therefore to understand atmospheric turbulence effects on vertical FSO communication links such as space-to-ground links, it is necessary to specify C_n^2 profiles along the atmospheric propagation path. To avoid the limitations on the applicability of classical approaches, propagation simulation through geometrical ray tracing is applied. This is achieved by considering the atmosphere along the optical propagation path as a spatial distribution of spherical bubbles with varying relative refractive index deviations representing turbulent eddies. The relative deviations of the refractive index are statistically determined from altitude-dependent and time varying temperature fluctuations, as measured by a microwave profiling radiometer. For each representative atmosphere ray paths are analyzed using geometrical optics, which is particularly advantageous in situations of strong turbulence where there is severe wavefront distortion and discontinuity. The refractive index structure parameter is then determined as a function of height and time.

Keywords: Atmospheric turbulence, Optical propagation, Profiling radiometer, Turbulence theory, Geometrical ray model, Bubble model

1. INTRODUCTION

Inhomogeneities in the refractive index of the atmosphere due to fluctuations of temperature, and to a lesser extent pressure, can significantly degrade the performance of free-space optical (FSO) communications links. Specifically the presence of turbulence can lead to spatio-temporal power fades and surges, as well as deleterious effects on spatial coherence, beam wander, beam broadening, etc.[1–5] The level of turbulence is highly dependent upon vertical height, therefore to properly assess vertical FSO communication links such as space-to-ground links, estimates of turbulence along the vertical propagation path must be specified. It has been shown previously that the determination of refractive index structure function C_n^2 profiles, important for the assessment of optical communications links, can theoretically be obtained from temperature data as measured by a microwave profiling radiometer, and the technique was applied to measured data with good results.[6] However, a complicating factor in application of the theoretical expressions involved is that the parameter values required in the spectral analysis may vary over several orders of magnitude necessitating very careful determination of the break frequency k_u, which separates the buoyancy subrange from the inertial subrange.

Here a computational method is applied that does not require additional parameter estimates beyond what is available experimentally. To accomplish this we simulate beam propagation through a turbulent medium through geometric ray tracing, and determine C_n^2 from cross-correlations of the ray distributions on the image plane as in time-lapse imagery.[7,8] The distance from the ray source to the image plane corresponds to the vertical height of interest. The propagation medium is modeled by spherical bubbles with varying refractive index deviations representing turbulent eddies.[9] Measured temperature profiles are used to generate corresponding refractive index distributions with which to assign values to the bubbles. In this way the fluctuations are related statistically to the measured profiles.

Send correspondence to brian.e.vyhnalek@nasa.gov

2. METHOD DESCRIPTION

2.0.1 Spherical Bubble Model

Atmospheric turbulence is a condition due to small temperature perturbations which manifest optically as fluctuations in the local index of refraction leading to intensity scintillation, and manifest mechanically as local air mass density fluctuations. According to Kolmogorov and Richardson, the air mass perturbations due to temperature and wind velocity are described as vorticies or eddies of varying size extending from some maximum, or outer scale L_0, to a minimum inner scale l_0. Over this range, the inertial subrange, kinetic energy cascades through the turbulent eddies from L_0 to l_0 until finally the size scales involved are too small to have relevant structure and the energy is dissipated.[10]

A very effective and relatively simple method of simulating optical beam propagation through a turbulent medium is to model the turbulent eddies as spherical bubbles of varying refractive index[9,11–13] given by

$$n(\vec{r}_s) = n_{air} + \tilde{n}(\vec{r}_s), \tag{1}$$

where $\vec{r}_s$ is a point on or inside a sphere, $n_{air} \approx 1$ is the index of refraction of air at atmospheric pressure, and $\tilde{n}(\vec{r}_s)$ is a perturbation on the order of 10^{-4} or less. These spheres are assigned random sizes in the interval $[l_0, L_0]$ corresponding to the inertial subrange, and are distributed randomly throughout a volume. A distribution of rays, typically uniform or Gaussian, is defined at a source plane and propagated according to geometrical optics through the assortment of spheres until each ray intersects the image plane at some distance of interest (Fig. 1).

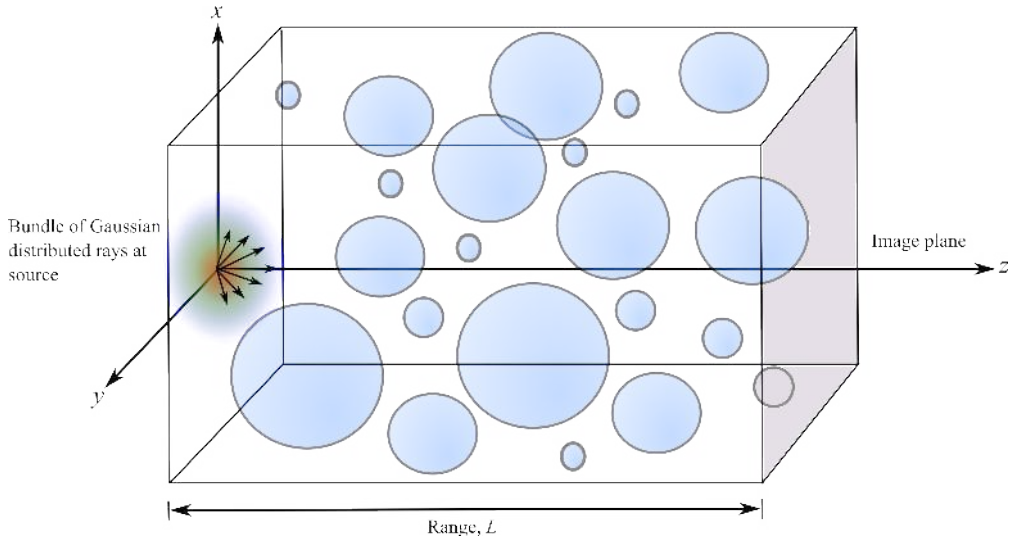

Figure 1: Bubble model.[11]

2.0.2 Geometric Ray Tracing

The ray tracing process is straightforward, being primarily repeated applications of Snell's law. As depicted in Fig. 2, each ray $\vec{P}$ is represented as a vector sum of an origin vector $\vec{P}_0$ and a unit direction vector $\vec{v}$ multiplied by a parameter t,

$$\vec{P} = \vec{P}_0 + t\hat{v}, \tag{2}$$

and similarly each sphere (or turbulent eddy bubble) is specified by a point on the sphere $\vec{P}$, a center $\vec{C}$, and a radius r,

$$||\vec{P} - \vec{C}||^2 - r^2 = 0. \tag{3}$$

The intersection of a ray with a sphere is determined by substituting Eq. (2) into (3) and solving for the parameter t giving

$$t = -(\vec{P}_0 - \vec{C}) \cdot \vec{v} \pm \sqrt{[(\vec{P}_0 - \vec{C}) \cdot \vec{v}]^2 - [(\vec{P}_0 - \vec{C})^2 - r^2]}, \tag{4}$$

where t must be real and the smallest non-negative value must be taken. If there are no positive real roots, then an intersection has not occurred.

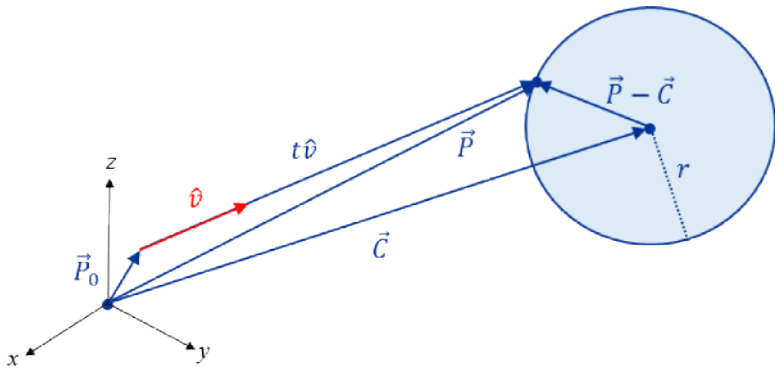

Figure 2: Ray-sphere intersection.

Once an intersection has been determined, refraction through the sphere must then be considered. For three-dimensional applications Snell's law is written in the vector form as

$$n_i(\hat{k}_i \times \hat{n}) = n_t(\hat{k}_t \times \hat{n}) \tag{5}$$

where n_i and n_t are the refractive indices of the respective incident and transmitted mediums, $\hat{n}$ is the unit normal to the sphere at the point of intersection, $\hat{n} = (\vec{P} - \vec{C})/||\vec{P} - \vec{C}||$, and $\hat{k}_i$ and $\hat{k}_t$ are the unit direction vectors of the incident and transmitted rays (Fig. 3a).

Since Eq. (5) can be written as

$$(n_i\hat{k}_i - n_t\hat{k}_t) \times \hat{n} = 0,$$

we can define a vector $\vec{\Gamma}$ such that

$$\vec{\Gamma} = \left[n_t(\hat{k}_t \cdot \hat{n}) - n_i(\hat{k}_i \cdot \hat{n})\right] \hat{n},$$

with the property that $\vec{\Gamma} \times \hat{n} = 0$, and it then follows that Eq. (5) becomes

$$n_i\hat{k}_i - n_t\hat{k}_t = n_i(\hat{k}_i \cdot \hat{n}) - n_t(\hat{k}_t \cdot \hat{n}). \tag{6}$$

From the fact that $\hat{k}_t \cdot \hat{n} = \cos\theta_t, \hat{k}_i \cdot \hat{n} = \cos\theta_i$, and Snell's law we have

$$(\hat{k}_t \cdot \hat{n})^2 = 1 - \left(\frac{n_i}{n_t}\right)^2 \left[1 - (\hat{k}_i \cdot \hat{n})^2\right],$$

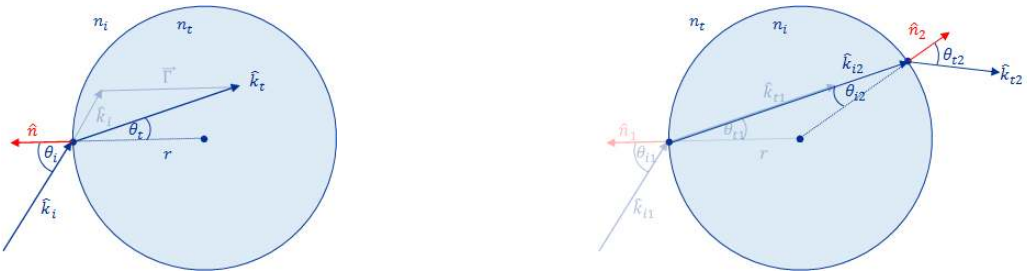

(a) Ray entering sphere (b) Ray exiting sphere

Figure 3: Ray refraction through a sphere.

which after taking the negative root (since $\hat{k}_t \cdot \hat{n} < 0$) and upon substitution into Eq. (6) can be solved readily for the refracted ray direction vector at the first interface

$$\hat{k}_{t,1} = \frac{n_i}{n_t}\hat{k}_i - \left[\left\{1 - \left(\frac{n_i}{n_t}\right)^2 \left[1 - (\hat{k}_i \cdot \hat{n})^2\right]\right\}^{\frac{1}{2}} + \frac{n_i}{n_t}(\hat{k}_i \cdot \hat{n})\right]\hat{n}. \tag{7}$$

The refracted ray point of intersection with the back side of the sphere is

$$\vec{P}_2 = \vec{P}_1 - 2r\left(\hat{k}_{t,1} \cdot \hat{n}_1\right)\hat{k}_{t,1} \tag{8}$$

where $\vec{P}_1$ is the first intersection point, $\hat{k}_{t,1}$ is given by Eq. (7), and $\hat{n}_1$ is the unit normal at the first intersection. Similar to before, the ray direction vector exiting the sphere at the second interface is given by

$$\hat{k}_{t,2} = \frac{n_i}{n_t}\hat{k}_i + \left[\left\{1 - \left(\frac{n_i}{n_t}\right)^2 \left[1 - (\hat{k}_i \cdot \hat{n})^2\right]\right\}^{\frac{1}{2}} - \frac{n_i}{n_t}(\hat{k}_i \cdot \hat{n})\right]\hat{n}, \tag{9}$$

where in this case n_i and n_t have a reversed connotation than at the first interface, $\hat{k}_i = \hat{k}_{t,1}$ and $\hat{n}$ is the unit normal at the sphere exit, $\hat{n} = (\vec{P}_2 - \vec{C})/||\vec{P}_2 - \vec{C}||$. The point $\vec{P}_2$ becomes the new ray origin and $\hat{k}_{t,2}$ becomes the new ray direction unit vector (Fig. 3b). The process is repeated for each ray and intersecting spheres until all the rays have been propagated to the viewing plane.

2.0.3 Connecting with C_n^2

The ray distribution on the viewing plane forms an image whose frame-to-frame variance in time can be related to C_n^2 through the angular tilt variance $\langle\alpha^2\rangle$, where α is the z-tilt when viewing a source in the direction θ. Since the frame-to-frame motion of each image is independent, the angular tilt variances $\langle\alpha_{x,y}^2\rangle$ in the x and y directions are essentially equivalent to the frame-to-frame intensity variances $\langle I_{x,y}^2\rangle$ in each respective direction except for a scale factor related to pixel size Δp and camera focal length f. For simulation purposes this scale factor can be chosen arbitrarily by defining an appropriate focal length. It follows that[7]

$$\langle\alpha_{x,y}^2\rangle = 0.5\frac{\Delta p}{f}\langle I_{x,y}^2\rangle, \tag{10}$$

and

$$\langle\alpha^2\rangle = \langle\alpha_x^2\rangle + \langle\alpha_y^2\rangle. \tag{11}$$

Finally, path-averaged estimates of the refractive index structure factor C_n^2 can be determined from the relation

$$\langle\alpha^2\rangle = C_n^2 \int_0^L f_\alpha(z)dz, \tag{12}$$

in which L is the propagation length, and $f_\alpha(z)$ is a path weighting function given by[7]

$$f_\alpha(z) = -5.82\left(\frac{16}{\pi}\right)^2 D^{-1/3}\int_0^\infty xe^{-2x^2}dx\int_0^{2\pi}\int_0^1 \left[\left(u\cos^{-1}u\right) - u^2\left(3 - 2u^2\right)\sqrt{(1-u^2)}\right] \times \left[u^2\left(1 - \frac{z}{L}\right)^2 + \left(\frac{zd}{DL}x\right)^2 + 2u\left(1 - \frac{z}{L}\right)\left(\frac{zd}{DL}x\right)\cos\theta\right]^{5/6} du\, d\theta, \tag{13}$$

where D is the imaging aperture size, $d = \Delta p$ is the pixel size, L is the path length, and $z = 0$ is at the image plane.

3. DETERMINATION OF REFRACTIVE INDEX STATISTICS FROM RADIOMETER TEMPERATURE MEASUREMENTS

Temperature and humidity profiles were taken throughout 2013 at the NASA TDRSS White Sands ground terminal site near Las Cruces, NM using a Radiometrics Corporation MP-3000A multifrequency microwave profiling radiometer (MWR) pointed to zenith (Fig. 4). This radiometer features[14] in total 35 calibrated channels of 300 MHz bandwidth each, with 21 K-band channels (22 - 30 GHz) and 14 V-band channels (51 - 59 GHz). Each channel has a 1.1 second integration time giving a total acquisition period of $\Delta t \approx 40$s per sample, yielding about 2,160 data samples per day per height.

Figure 4: Radiometrics Corp. MP-3000A MWR at White Sands, NM.

Since humidity fluctuations do not contribute at optical wavelengths[10] only temperature profiles are considered. Figure 5 shows an example temperature time series and Figure 6 shows a one day-averaged temperature profile. A linear fit gives the slope of the temperature profile as approximately -7.0 K/km.

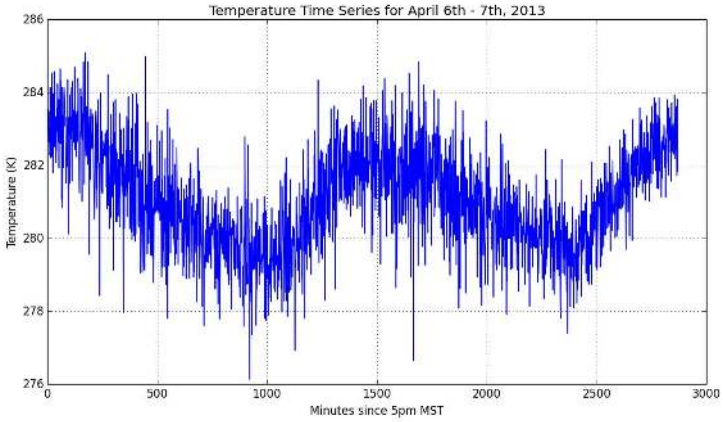

Figure 5: Temperature time series at $h = 1.5$ km for April 6th - 7th, 2013.

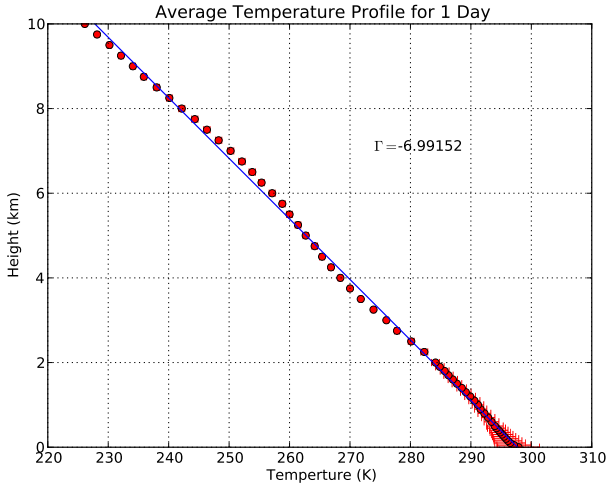

Figure 6: Single day average temperature profile (April 6th, 2013).

The fluctuating refractive index of air at position $\vec{r}$ and time t can be determined from temperature and pressure fluctuations through the relationship[15]

$$n(\vec{r},t) = 1 + 79 \times 10^{-6} \frac{P(\vec{r},t)}{T(\vec{r},t)} \tag{14}$$

where P is the pressure in millibars and T is the temperature in kelvin. Pressure fluctuations can be considered negligible,[15] thus $P(\vec{r},t) \approx \langle P(\vec{r}) \rangle$, and pressure profiles were assumed to follow an exponential barometric model parameterized by available ground measurements and the temperature profile data.

For each temperature time series at a given height, a corresponding refractive index time series was calculated from Eq. (14) and a 10 s moving average was also determined (Figure 7). The moving average was then removed (Figure 8), and a Gaussian distribution was fit to the reduced data (Figure 9).

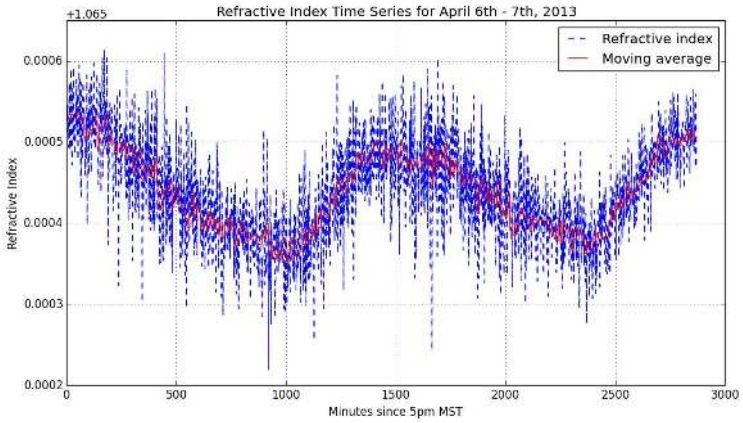

Figure 7: Refractive index time series.

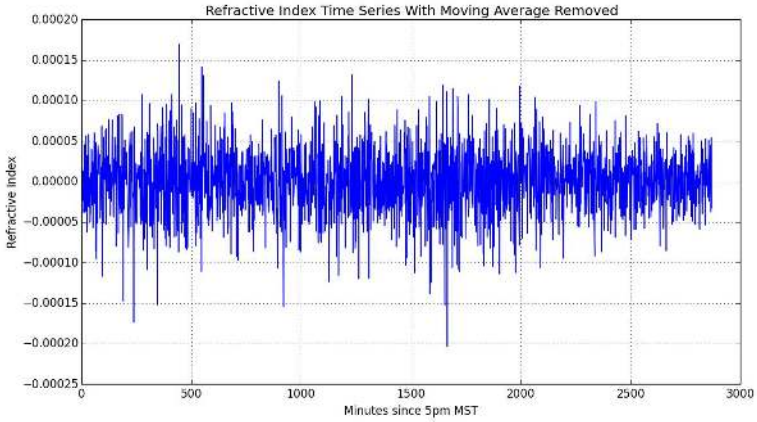

Figure 8: Time series with moving average removed.

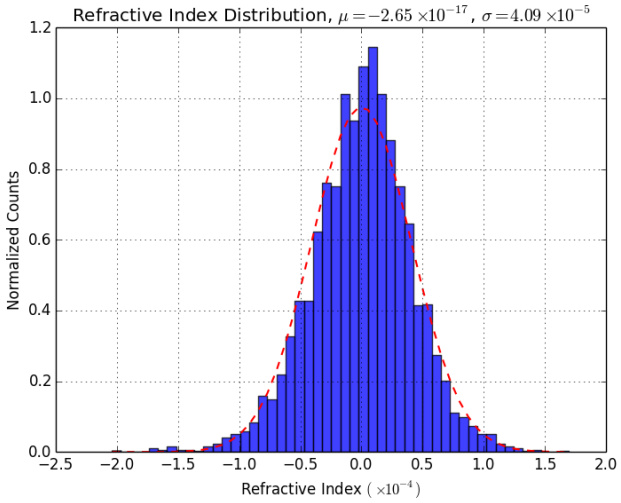

Figure 9: Histogram with Gaussian fit.

4. APPLICATION OF THE METHOD AND RESULTS

A single data set is comprised of about 2,160 time samples for 58 different heights from a ground height of 1.472 km to a maximum altitude 10 km above. For each time series corresponding to a single day and height the refractive index distribution was determined. A source ray bundle of approximately 1×10^6 collimated rays with a Gaussian intensity distribution of $\sigma = 100$ cm was generated and used as the source for all runs of the simulation program (Figure 10). The computational volume was bounded in the x and y directions to the interval [-5 m, 5 m] and in the z direction as 50 m, 100 m, or 250 m depending on the altitude interval of the radiometer.

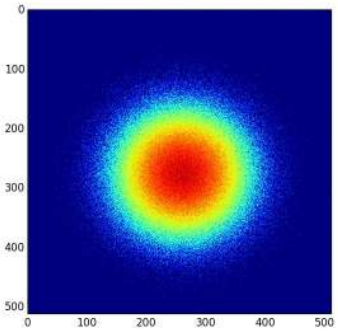

Figure 10: Initial ray distribution on a 512×512 grid.

The source rays were propagated through 2,048 spheres with refractive indices determined by generating a normally distributed random number from the distribution as described above, and then adding back the appropriate moving average value. Example output images are shown in Figure 11.

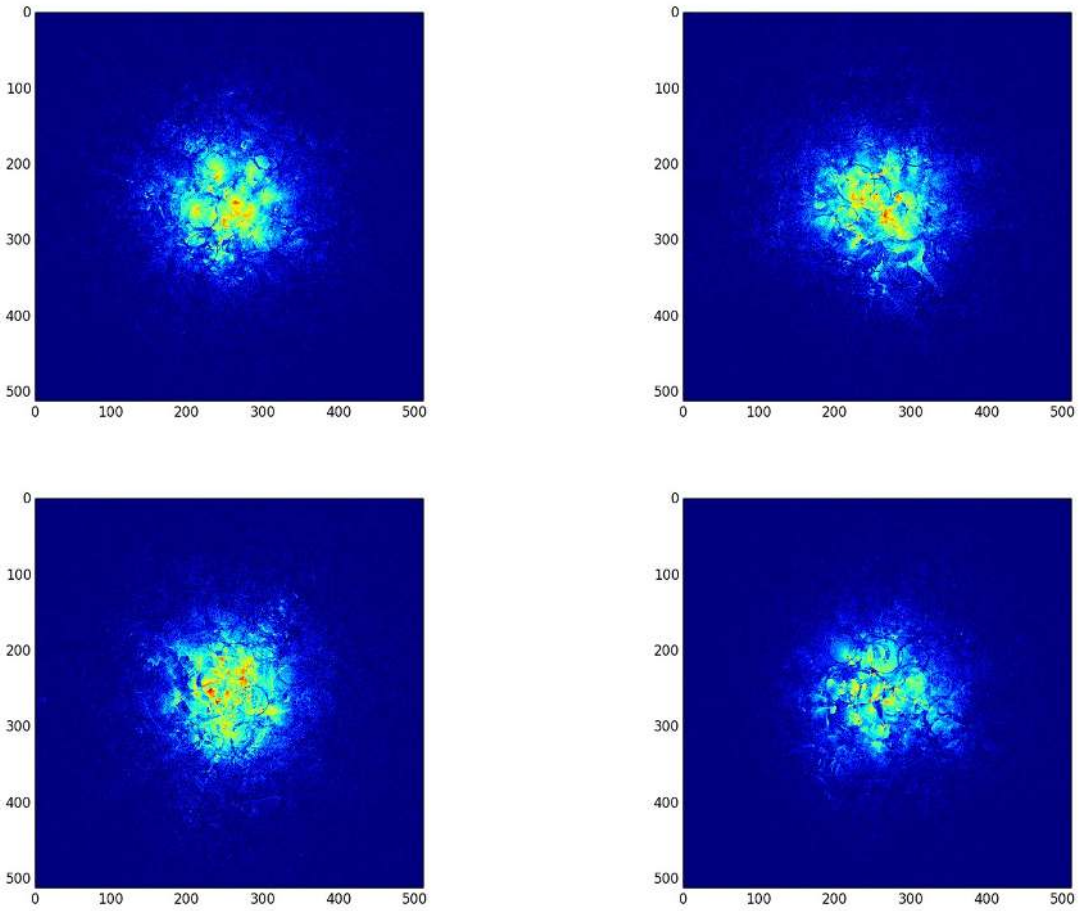

Figure 11: Example image plane ray distributions for $h = 250$ m at different times.

In all 576 images were generated for each height. Ideally an image would have generated for each time sample, but this was not possible due to prohibitively long computation time. The cross-correlations between subsequent images was calculated from which the image shift variance was determined. After applying Eq (10) - Eq (13) with $\Delta p = 0.02$, $D = 7.07$ m, and $f = 0.5 \times \Delta p$ estimates of the refractive index structure factor were obtained. The estimates were averaged over 4 samples corresponding to the 10-min averaging of the measurement data, giving 144 points for a particular height per day. Figure 12 shows a representative output of the algorithm at a height of 250 m above ground and Figure 13 shows the average C_n^2 profile for the day, plotted with the Hunfagel-Valley model with a value of $v = 27$ m/s for the high altitude wind velocity parameter.[10]

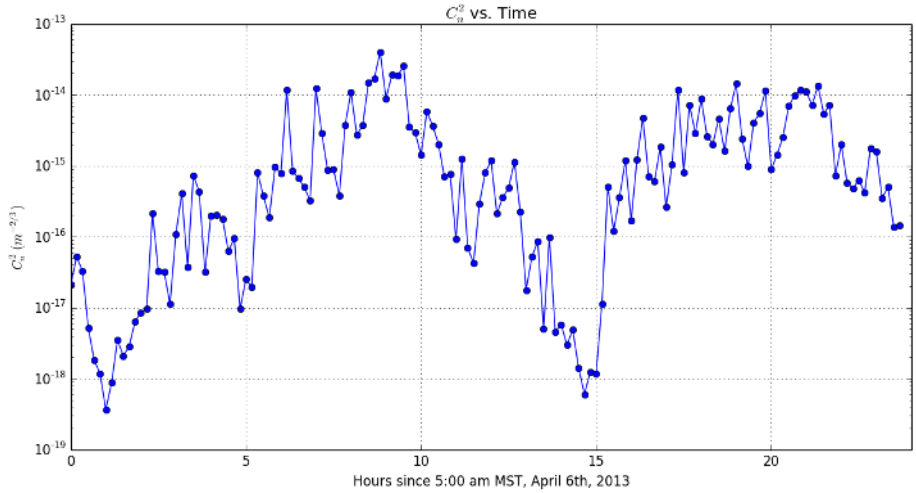

Figure 12: C_n^2 for April 6th, 2013 at 250 m above ground level. Each point is a ten-min average.

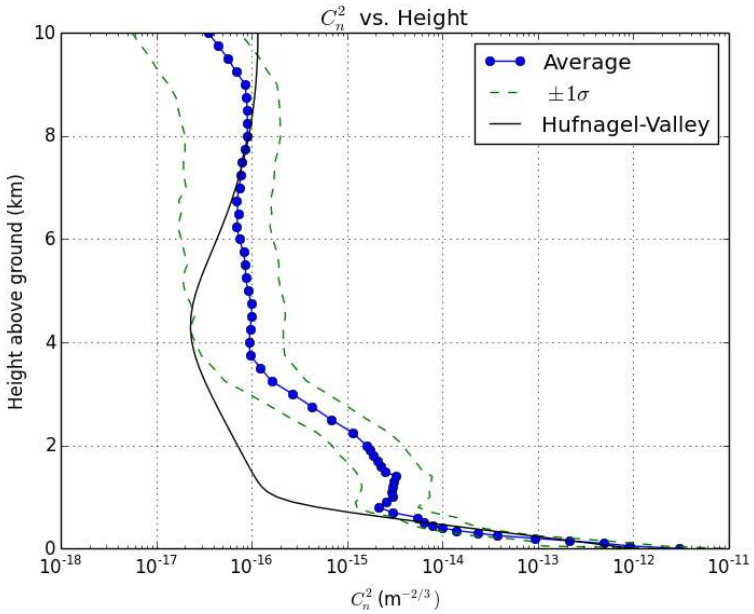

Figure 13: Average C_n^2 profile for April 6th, 2013.

The results near ground height show a clear diurnal cycle with minimum values on the order of 10^{-18} $m^{-2/3}$ near sunrise and sunset, with a peak value of about 4×10^{-14} $m^{-2/3}$ near midday. The profile results show a strong dependence of C_n^2 on altitude for heights less than 1 km, spanning nearly four orders of magnitude from about $10^{-11}m^{-2/3}$ to values nearly on the order of $10^{-15}m^{-2/3}$, agreeing well with the Hufnagel-Valley model. Above 1 km the height dependence lessens before diminishing substantially above 4 km where C_n^2 values are generally in the range of 10^{-16}.

5. CONCLUSIONS

A computational method using geometrical ray tracing and techniques of time-lapse imagery was applied for obtaining C_n^2 profiles from microwave profiling radiometer temperature measurements. Reasonable values were obtained and good agreement with an established model was shown. A particular advantage of this method is that the specific form of C_T^2, the temperature structure parameter, is not required - in particular for altitudes less than 1 km or so near the ground where the Kolmogorov "2/3 law" may not hold. Additionally, sensitive parameter values such as the buoyancy to inertial subrange crossover frequency are not needed. The phase-based nature of this computational method also has the advantage of being applicable in regimes of strong turbulence. Future applications of this method would benefit from computational speed-up techniques, such as implementation on a graphics processing unit (GPU) for which ray tracing is highly suitable.

ACKNOWLEDGMENTS

The author would like to acknowledge the support given by the NASA Space Communications and Navigation (SCaN) Integrated Radio and Optical Communications (iROC) project.

REFERENCES

1. R. Lawrence and J. Strohbehn, "A survey of clear-air propagation effects relevant to optical communications," *Proc. IEEE* **58**, pp. 1523–1545, Oct. 1970.
2. R. Fante, "Electromagnetic beam propagation in turbulent media," *Proc. IEEE* **63**, pp. 1669–1690, 1975.
3. V. Zuev, *Laser Beams in the Atmosphere*, Consultants' Bureau, New York, 1982.
4. X. Zhu and J. M. Kahn, "Free-space optical communications through atmospheric turbulence channels," *IEEE Transaction on Communications* **50**, pp. 1293–1300, Aug. 2002.
5. A. Ishimaru, "Fluctuations of a beam wave propagating through a locally homogeneous medium," *Radio Sci.* **4**, pp. 295–305, 1969.
6. R. M. Manning and B. Vyhnalek, "A microwave radiometric method to obtain the average path profile of atmospheric turbulence and humidity structure parameters and its application to optical propagation system assessment," in *Proc. SPIE 2015, 9354, 935406*, 2015.
7. S. Basu, J. E. McCrae, and S. T. Fiorino, "Estimation of the path-averaged atmospheric refractive index structure constant from time-lapse imagery," in *Proc. SPIE 2015, 9465, 94650T*, 2015.
8. S. Basu, J. McCrae, and S. Fiorino, "Estimation of atmospheric refractive index gradient variations and cn2 from time-lapse imagery," in *Propagation Through and Characterization of Atmospheric and Oceanic Phenomena*, Optical Society of America, 2016.
9. H. Yuskel and C. Davis, "A geometrical optics approach for modeling aperture averaging in free space optical communications applications," in *Proc. SPIE 2006, 6303, 630302*, 2006.
10. R. Beland, "Propagation through atmospheric optical turbulence," in *The Infrared and Electro-Optical Systems Handbookm Vol. 2 - Atmospheric Propagation of Radiation*, F. Smith, ed., SPIE Optical Engineering Press, Bellingham, WA, 1993.
11. D. Yuskel and H. Yuskel, "Geometrical monte carlo simulation of atmospheric turbulence," in *Proc. SPIE 2013, 8874, 88740U*, 2013.

12. D. Yuskel and H. Yuskel, "Geometrical modeling of optical phase difference for analyzing atmospheric turbulence," in *Proc. SPIE 2013, 8874, 88740W*, 2013.
13. C. Wu and C. C. Davis, "Geometrical optics analysis of atmospheric turbulence," in *Proc. SPIE 2013, 8874, 88740V*, 2013.
14. Radiometrics Corp., *Profiler Operator's Manual*, March 2008.
15. L. C. Andrews and R. L. Phillips, *Laser beam propagation through random media*, vol. 152, SPIE Press, 2005.